Collisional effects in the blue wing of Lyman-α

Fernand Spiegelman, N. F. Allard, J. F. Kielkopf

A&A 651, A51 (2021)
https://doi.org/10.1051/0004-6361/202140681

Astronomy & Astrophysics

Collisional effects in the blue wing of Lyman-α

F. Spiegelman[1], N. F. Allard[2,3], and J. F. Kielkopf[4]

[1] Laboratoire de Physique et Chimie Quantique, Université de Toulouse (UPS) and CNRS, 118 route de Narbonne, 31400 Toulouse, France
[2] GEPI, Observatoire de Paris, Université PSL, UMR 8111, CNRS, 61 avenue de l'Observatoire, 75014 Paris, France
e-mail: nicole.allard@obspm.fr
[3] Sorbonne Université, CNRS, UMR7095, Institut d'Astrophysique de Paris, 98bis boulevard Arago, Paris, France
[4] Department of Physics and Astronomy, University of Louisville, Louisville, Kentucky 40292, USA

Received 28 February 2021 / Accepted 12 April 2021

ABSTRACT

Spectral observations below Lyman-α are now obtained with the Cosmic Origin Spectrograph (COS) on the *Hubble* Space Telescope. It is therefore necessary to provide an accurate treatment of the blue wing of the Lyman-α line that enables correct calculations of radiative transport in DA and DBA white dwarf stars. On the theoretical front, we very recently developed very accurate H-He potential energies for the hydrogen 1s, 2s, and 2p states. Nevertheless, an uncertainty remained about the asymptotic correlation of the Σ states and the electronic dipole transition moments. A similar difficulty occurred in our first calculations for the resonance broadening of hydrogen perturbed by collisions with neutral H atoms. The aim of this paper is twofold. First, we clarify the question of the asymptotic correlation of the Σ states, and we show that relativistic contributions, even very tiny, may need to be accounted for a correct long-range and asymptotic description of the states because of the specific 2s 2p Coulomb degeneracy in hydrogen. This effect of relativistic corrections, inducing small splitting of the 2s and 2p states of H, is shown to be important for the Σ-Σ transition dipole moments in H-He and is also discussed in H-H. Second, we use existent (H-H) and newly determined (H-He) accurate potentials and properties to provide a theoretical investigation of the collisional effects on the blue wing of the Lyman-α line of H perturbed by He and H. We study the relative contributions in the blue wing of the H and He atoms according to their relative densities. We finally achieve a comparison with recent COS observations and propose an assignment for a feature centered at 1190 Å.

Key words. line: profiles – atomic data – white dwarfs – molecular data

1. Introduction

In helium-dominated white dwarfs, the discrepancy in the hydrogen abundance between Balmer-α from the optical data and Lyman-α from the ultraviolet (UV) data is strong. In addition, the Lyman-α line profile is asymmetric (see Xu et al. 2017, and references therein). The existence of a quasi-molecular line satellite is crucial for understanding this asymmetrical shape of the Lyman-α line observed with the Cosmic Origin Spectrograph (COS; see Fig. 1 in Allard et al. 2020). This absorption feature has been predicted by detailed collisional broadening profiles by Allard & Christova (2009). These authors made an exhaustive study of the red wing of the Lyman-α line perturbed by H-He collisions. They considered high He densities met in cool DZ white dwarfs and examined the validity range of the one-perturber approximation that is widely used to calculate the line wings. H-He potentials were theoretically determined by several authors, namely Theodorakopoulos et al. (1984, 1987), Sarpal et al. (1991), Lo et al. (2006), Belyaev (2015), and Allard et al. (2020). Allard & Christova (2009) used the potentials and dipole moments of Theodorakopoulos et al. (1984, 1987), but were limited by a lack of accuracy of the molecular potential of the $C\Sigma$ state. They noticed an unexpected well of about 150 cm^{-1} at $R \sim 8$ Å that is related to the choice of basis functions. Significant progress in the description of the H-He potential energies has been achieved in a recent work (Allard et al. 2020) using extensive basis sets and multi-reference configuration interaction (MRCI) calculations (Knowles & Werner 1992; Werner et al. 2015) to determine accurate ab initio potential energy curves. Nevertheless, because of the specific degeneracy of the hydrogen levels in the Coulomb model, the adiabatic correlation of the A and C states to either 2s (dipole forbidden from the ground state) or 2p (allowed) states is not fully characterized using the Coulomb Hamiltonian only. Relativistic effects that are smaller than 1 cm^{-1} for hydrogen are responsible for lifting the strict degeneracy of the hydrogen atomic levels in the Coulomb model (Kramida 2010). This level splitting is crucial for establishing the adiabatic correlation of the molecular states toward the asymptotic levels, and thus the specific asymptotic behavior of the dipole transition moments from the ground state. Thus, one aspect of the present paper is to redetermine and rediscuss the ground and lowest excited potential energy curves (PECs) of H-He and the electric transition dipole moments (Sect. 2.1), with a stronger focus on their long-distance behavior. A detailed correlation to the dissociated atomic states and its effect on the transition dipole moments is specifically discussed in Sect. 2.2. We consider spin-orbit (SO) coupling in Sect. 2.3.

A similar asymmetry as in the Lyman-α H-He line profile also exists in the resonance broadening of hydrogen perturbed by collisions with H atoms. In our first calculations for the resonance broadening of hydrogen perturbed by collisions with H and H^+ (Allard et al. 1994), we were mainly interested in quasi-molecular absorption of transient H_2 and H_2^+ molecules in the far red wing of Lyman-α. Singlet states of H_2 lead to line satellites from the free-free transitions $B^1\Sigma_u^+ \rightarrow X^1\Sigma_g^+$ and $C^1\Pi_u \rightarrow X^1\Sigma_g^+$. These states also are responsible for the bound-bound Lyman and

Werner H_2 bands. Triplet states only lead to a blue asymmetry because of a close line satellite that appears as a shoulder in the blue wing. These improved theoretical calculations of the complete Lyman-α profile including both red and blue wings were applied to the interpretation of International Ultraviolet Explorer (IUE) and *Hubble* Space Telescope (HST) spectra. They were shown to be fundamental in the interpretation of UV spectra of variable DA white dwarfs (ZZ Ceti stars; Koester et al. 1994). The analysis of the Lyman-α satellites in the far red wing is not only a way to establish the location of the ZZ Ceti instability of variable DA white dwarfs, but also a test of the assumptions about convection efficiency (Bergeron et al. 1995).

The correlation diagram for H_2 states contributing to Lyman-α shown in Table 2 of Allard et al. (1994) was not correct because of an error in the preliminary ab initio calculations of the $^3\Sigma_g^+$-$^3\Sigma_u^+$ transition moments. This error was noted in Allard et al. (1998a), who pointed out that the variation of the radiative dipole moment must be included in the line profile calculation. A new correlation diagram was presented in Allard & Kielkopf (2009) to correct Table 2 of Allard et al. (1994). This correlation diagram has been used in Allard et al. (1998a) and in our subsequent work. Electronic transition moments among singlets and triplets computed by Spielfiedel (2003) and Spielfiedel et al. (2004) were used in Allard & Kielkopf (2009) for an exhaustive study of the red wing of Lyman-α in order to determine the contribution of the triplet transition $b^3\Sigma_u^+ \rightarrow a^3\Sigma_g^+$ that was not considered in Allard et al. (1994). Although we never clarified the correct contribution of triplet states to the blue wing of the Lyman-α line, a blue line satellite was observed in experimental spectra (Kielkopf & Allard 1995, 1998).

We discuss the effect of the 2s-2p degeneracy lifting on the long-distance behavior of H_2 states in Sect. 2.4. In Sect. 3 we present a study of the blue wing of the Lyman-α line perturbed by collisions with H and He atoms in order to examine their relative contributions in the Lyman-α spectrum.

2. Diatomic potentials and electronic transition dipole moments

The transient interactions of atoms during radiative collisions are the main physical quantities needed for a good understanding of the effect of collisional processes on radiative transfer in stellar atmospheres and the spectra emitted by white dwarf stars. We consider herafter H-He with and without spin-orbit coupling and H-H.

2.1. H-He without SO coupling

The ab initio calculations of the potentials were carried out with the MOLPRO package (Werner et al. 2015) using a very large Gaussian basis set that was initially taken from the *spdfgh* aug-cc-pV6Z basis set of the MOLPRO library for both He and H atoms, complemented by additional diffuse functions. On both He and H, the aug-cc-pV6Z Gaussian basis set was complemented by diffuse functions in each l manifold. The added exponents on He were the same as in the previous work of Allard et al. (2020). A slightly larger complementary set of functions was determined and used on H in order to accurately describe the atomic spectrum of hydrogen up to $n = 4$, with both diffuse functions and intermediate exponents improving the nodal structure (Table A.2). Thus the basis set includes 239 Gaussian functions on He and 297 on H.

A unique set of molecular orbitals was obtained from a relativistic Hartree-Fock (RHF) calculation of HeH^+, incorporating the scalar relativistic effects (Darwin and mass-velocity contributions) within the Douglas-Kroll-Hess (DKH) scheme (Reiher 2006; Nakajima & Hirao 2011) at second order. The virtual orbitals of HeH^+ provide relevant excited molecular orbitals that properly dissociate into the exact orbitals of H (as represented within the present basis). All subsequent calculations include the DKH contributions. The configuration interaction (CI) was generated by a primary complete active space (CAS) including 14, 7, 7, and 4 molecular orbitals in each of the a_1, b_1, b_2, and a_2 manifolds of the C_{2v} point group. This ensured that all Σ^+, Π, Δ, and Φ states dissociating up to $n = 4$ were properly described in the CAS space. Finally, an MRCI calculation (Knowles & Werner 1992) generated from this CAS space was conducted for the A_1, B_1, and A_2 manifolds with 13, 7, and 3 eigenstates, respectively. Although we only discuss the Lyman-α contribution here, the relevant electric dipole transition moments corresponding to Lyman and Balmer transitions up to $n = 4$ were determined in the same calculations and will be the object of future publication. Relativistic effects are obviously very tiny on hydrogen. Nevertheless, because all excited levels present degeneracy in the simple nonrelativistic Coulomb scheme, it may be important for a correct long-range description to account even for very tiny splitting.

The DKH contribution, which is essentially active in the inner parts of the wave functions close to the atoms, splits the degenerate components of a given n and stabilizes more significantly the low l levels. It also slightly increases the excitation energies from the 1s level. In the present work that is concerned with the 2s, 2p states, these scalar contributions were complemented by accounting for spin-orbit coupling with similar magnitude. For all levels of H n = 1–4, the use of the extensive basis set and inclusion of the DKH correction provides transition energies obtained with an accuracy better than 0.5 cm^{-1} compared to the experimental atomic data (Kramida et al. 2020). Table 1 illustrates the achieved accuracy (in particular, the ordering of the 2s, 2p states) that is important to determine the configurational mixings that span the molecular states and the resulting transition probabilities that contribute to Lyman-α.

Table 1. Atomic energy levels of hydrogen (in cm^{-1}).

Level	Coulomb /DKH	Coulomb/DKH/mass	Experimental
1s	0	0	0
2s	82 303.923	82 259.124	82 258.954
$2p_{3/2}$			82 259.285
$2p_{1/2}$			82 258.917
2p	82 304.240	82 259.440	82 259.163
3s	97 545.453	97 492.357	97 492.222
3p	97 545.607	97 492.511	97 492.293
3d	97 545.773	97 492.678	97 492.341
4s	102 880.238	102 824.234	102 823.853
4p	102 880.304	102 824.304	102 823.882
4d	102 880.366	102 824.368	102 823.903
4f	102 880.882	102 824.881	102 823.914

Notes. Columns are: theoretical levels including the DKH contribution (second column), theoretical levels with DKH contribution and finite proton mass correction (third column), experimental values (fourth column) taken from Kramida et al. (2020). Experimental values generally indicate the weighted average over the spin-orbit components, except for the 2p level, for which fine structure is explicitely detailed.

Table 2. Symmetry and labeling of molecular states dissociating into H(2s,2p)+He and H(2s,2p)+H.

Dissociation	Molecular state
$He(1s^2)+H(1s)$	$X^2\Sigma^+$
$He(1s^2)+H(2s,2p)$	$C^2\Sigma^+$, $A^2\Sigma^+$, $B^2\Pi$
$H(1s)+H(1s)$	$X^1\Sigma_g^+$, $b^3\Sigma_u^+$
$H(1s)+H(2s,2p)$	$EF^1\Sigma_g^+$, $B'^1\Sigma_u^+$, $h^3\Sigma_g^+$, $e^3\Sigma_u^+$
	$GK^1\Sigma_g^+$, $B^1\Sigma_u^+$, $a^3\Sigma_g^+$,
	$f^3\Sigma_u^+$, $I^1\Pi_g$, $C^1\Pi_u$, $i^3\Pi_g$, $c^3\Pi_u$

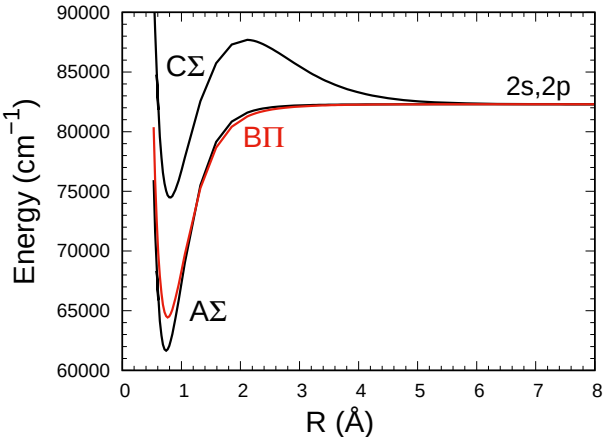

Fig. 1. MRCI adiabatic potential energy curves of H-He correlated with the 2s, 2p atomic levels. The zero energy corresponds to H(1s)+He($1s^2$) at dissociation.

The symmetry and labeling of the molecular states that dissociate into He($1s^2$) + H(2s,2p) is shown in Table 2, and their potential energy curves are plotted in Fig. 1. States $A\Sigma$ and $B\Pi$ are attractive with a minimum located around $R = 0.75$ Å. State $C^2\Sigma^+$ presents a repulsive character at medium and long range, resulting in a barrier and a shallower short-distance well depth. This medium-range repulsion is associated with the repulsion between the electronic density of the 2s and $2p_\sigma$ hydrogen orbitals along the axis and the electrons of the helium atom.

2.2. H-He PECs and correlation to dissociated atomic states

For distances smaller than 8.1 Å, the results we show in Fig. 1 do not differ substantially from the recent calculation of Allard et al. (2020), which was essentially achieved with a similar methodology. We used the same aug-cc-pV6Z basis set complemented with diffuse functions (the same functions for helium, and slightly more diffuse functions on hydrogen), and a larger CAS space generating the MRCI (three electrons in 32 orbitals, instead of three electrons in 14 orbitals in the former work). None of these differences are expected to provide significant quantitative changes at short distance concerning the ground state and the states dissociating into H($n = 2$)+He. However, no explicit mention of the relativistic effects was made in Allard et al. (2020), and the C state potential energy curve was found to converge to the unique Coulomb 2s/2p asymptote with a dipole moment for the $X - C$ transition that vanished asymptotically, meaning an adiabatic correlation of the obtained C state with the dipole-forbidden 2s atomic state. Conversely, the transition

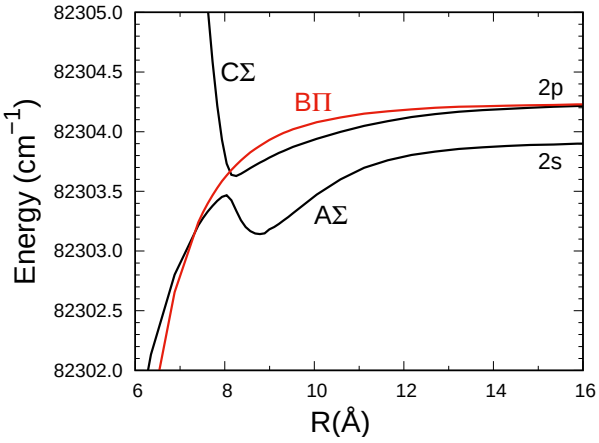

Fig. 2. Long range zoom of the MRCI adiabatic H-He potential energy curves of states A, B and C dissociating into H($n = 2$)+He. The zero energy corresponds to H(1s)+He($1s^2$) at dissociation.

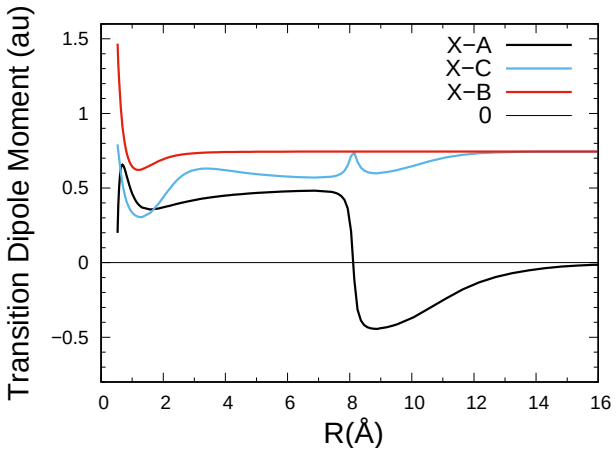

Fig. 3. Spin-orbit-less transition dipole moments of H-He from the X ground state toward the adiabatic A, B, and C states of H-He.

dipole moment $X - A$ was found to converge to that of the atomic 1s-2p transition dipole moment value.

We here focus strongly on the medium and long distance of the potential curves, detailed in Fig. 2. In particular, at the asymptotic limit, the DKH relativistic correction lifts the hydrogen 2s/2p degeneracy, lowering the 2s state more than the 2p state. This results in a 2s-2p splitting of 0.316 cm^{-1}. As a result, a long-distance avoided crossing around 8.1 Å occurs in the $^2\Sigma^+$ manifold between the lower adiabatic state correlated with 2s and the upper state correlated with 2p. The state correlated with 2s has a tiny well at 8.7 Å. This causes the adiabatic upper state (labeled C at short distance by spectroscopists) to correlate with the 2p asymptote, while state A is correlated with 2s. The examination of the dipole transition moments from the ground state, shown in Fig. 3, reveals a crucial implication. This long-range avoided crossing induces a kink at 8.1 Å in the $X - C$ dipole moment and a sign change in the $X - A$ dipole transition moment. Moreover, both adiabatic states have transition moments that stabilize around 0.4–0.6 au below $R = 8.1$ Å, which means that the upper state loses some 2p character while the lower gains it, regardless of the avoided crossing at 8.1 Å. Thus, the situation results from a gradual 2s/2p mixing increasing with short distance, superimposed with the sharp avoidance at 8.1 Å.

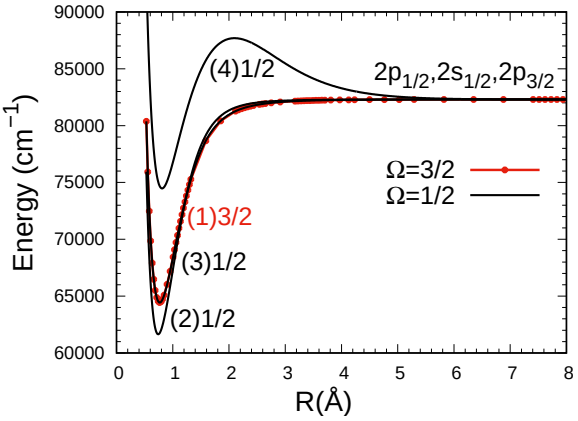

Fig. 4. Adiabatic H(n = 2)+He potential energy curves of molecular states including SO coupling. For better display, the red line of state (1)3/2 state is shown with superimposed dots. Zero energy corresponds to H(1s)+He(1s^2) at dissociation.

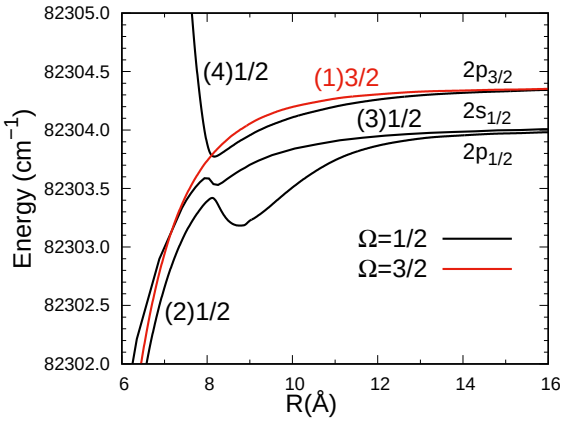

Fig. 5. Long-range zoom of the adiabatic potential energy curves of H(n = 2)+He states including SO coupling. Zero energy corresponds to H(1s)+He(1s^2) at dissociation.

2.3. H-He with SO coupling

SO coupling was incorporated following the atom-in-molecule-like scheme introduced by Cohen & Schneider (1974). It relies on an effective monoelectronic spin-orbit coupling operator,

$$H_{\rm SO} = \sum_i h_{\rm SO}(i) = \sum_i \zeta_i \hat{l}_i.\hat{s}_i, \tag{1}$$

where $\hat{l}$ and $\hat{s}$ are the orbital and spin-moment operators, and ζ_i is the effective spin constant associated with a given atomic electronic shell.

The total Hamiltonian $H_{\rm el} + H_{\rm SO}$ is expressed in the basis set of the eigenstates (here with total spin projection $\sigma = \pm\frac{1}{2}$) of the purely electrostatic Hamiltonian $H_{\rm el}$. Because the core electrons of He define a closed shell, the spin-orbit coupling between the molecular many-electron doublet states $\Psi_{k\sigma}$, approximated at this step as single determinants with the same closed shell $1s\sigma^2$ as the He subpart, is isomorphic to that between the singly occupied molecular spin-orbitals $\phi_{k\sigma}$, which are asymptotically correlated with the six 2p spin-orbitals and two 2s spin-orbitals of H. In its original formulation, the Cohen and Schneider approximation consists of assigning these matrix elements to their asymptotic (atomic) values. However, in the case of HeH, the 2s and 2p shells are asymptotically degenerate, which offers a favorable situation for electronic mixing. As previously mentioned, both adiabatic states $\Psi_{2s\Sigma}$ and $\Psi_{2p\Sigma}$ depart from their asymptotic character. Conversely, the $\Psi_{2p\Pi}$ state does not significantly mix with any other states and essentially conserves the asymptotic transition dipole moment from the ground state shown in Fig. 3.

In case of strong mixing, application of the Cohen and Schneider scheme is more relevant in a basis of diabatic or quasi-diabatic states, as has been discussed in previous works (Allard et al. 2020). Thus we determined $\Phi_{2s\Sigma}$ and $\Phi_{2p\Sigma}$ diabatic states through a unitary transform of the adiabatic states $\Psi_{2s\Sigma}$ and $\Psi_{2p\Sigma}$ and the constraint that the transition dipole moments from the ground state $X\ ^1\Sigma^+$ to the quasi-diabatic states at finite distance remain as close as possible to their asymptotic values, namely zero and 0.744 (asymptotic limit of the MRCI calculation),

$$\begin{pmatrix}\Phi_{2s\Sigma}\\ \Phi_{2p\Sigma}\end{pmatrix} = \begin{pmatrix}\cos\theta & -\sin\theta\\ \sin\theta & \cos\theta\end{pmatrix}\begin{pmatrix}\Psi_{2s\Sigma}\\ \Psi_{2p\Sigma}\end{pmatrix}. \tag{2}$$

Using this procedure, the transition dipole moments to the quasi-diabatic states are now exactly zero for state $\Phi_{2s\Sigma}$ and almost constant for state $\Phi_{2p\Sigma}$. The two latter, and state $\Phi_{2p\pi} = \Psi_{2p\Pi}$ considered as diabatic, therefore span the Cohen and Schneider spin-orbit matrix, the electronic Hamiltonian being nondiagonal in the Σ states manifold,

$$\langle\Phi_{k\sigma}|H_{\rm SO}|\Phi_{l\tau}\rangle = \langle\phi_{k\sigma}(\infty)|h_{\rm SO}|\phi_{l\tau}(\infty)\rangle. \tag{3}$$

The effective spin-orbit constant of the 2p shell of hydrogen is taken empirically as 2/3 times the spin-orbit splitting 0.366 cm^{-1}, namely ζ_{2p} = 0.244 cm^{-1} (Kramida et al. 2020). The total Hamiltonian matrix $H = H_{\rm el} + H_{\rm SO}$ for the n = 2 manifold is thus an 8 × 8 complex matrix that can decouple into real matrices according to different values of $\Omega = M_l + M_s$, where M_l and M_s are the orbital and spin moment projections on the molecular axis. For $\Omega = \pm1/2$ and $\Omega = \pm3/2$, these matrices read as follows:

$$\Omega = \pm1/2 \qquad \begin{pmatrix} E_{2s\Sigma} & V & 0\\ V & E_{2p\Sigma} & \zeta\sqrt{2}/2\\ 0 & \zeta\sqrt{2}/2 & E_{2p\Pi} - \zeta/2\end{pmatrix}$$

$$\Omega = \pm3/2 \qquad \left(E_{2p\Pi} + \zeta/2\right).$$

Here $E_{2s\Sigma}$ and $E_{2p\Sigma}$ are the energies of the quasi-diabatic states and V is their electronic coupling. $E_{2p\Pi}$ is the energy of the Π state. The diagonalization of the above matrix at each internuclear distance provides the spin-orbit eigenstates and energies. Despite being performed in an extensive basis, our calculation cannot reach sub cm^{-1} accuracy, which is required to investigate the molecular fine structure close to the asymptote because the SO splitting is only 0.366 cm^{-1}. In particular, the difference between the experimental atomic 2s state and the average of the 2p states is 0.209 cm^{-1}, while the calculation at separation yields 0.316 cm^{-1}. Thus we shifted the nonrelativistic diabatic potential $E_{2s\Sigma}$ upward by 0.107 cm^{-1}. As a consequence of SO splitting, the 2p$_{1/2}$ level now lies closely below the 2s$_{1/2}$ state, by 0.034 cm^{-1} in the calculation versus 0.035 cm^{-1} experimentally.

The molecular eigenstates can be labeled in adiabatic order in each Ω manifold, namely (2)1/2, (3)1/2, (4)1/2, and (1)3/2 above the ground state (1)1/2 (also named herafter $X_{1/2}$). Their potential curves are shown inf Figs. 4 and 5. They adiabatically correlate with atomic asymptotes 2p$_{1/2}$, 2s$_{1/2}$, 2p$_{3/2}$, and 2p$_{3/2}$, respectively. At short distance R < 1.2 Å, the lowest excited

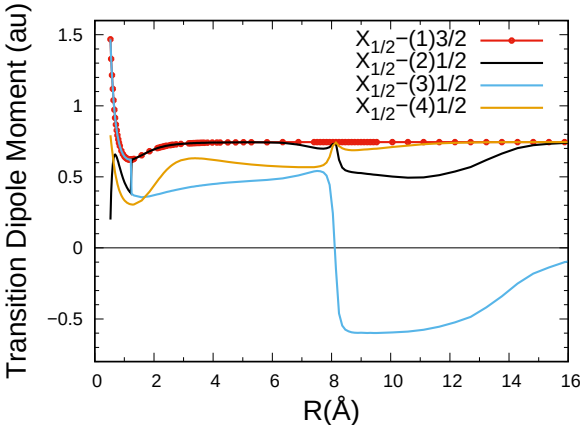

Fig. 6. Transition dipole moments from the $X_{1/2}$ ground state toward the adiabatic states dissociating into H(n = 2)+He including SO coupling. For better display, the red line of the $X_{1/2} - (1)3/2$ transition dipole moment is shown with superimposed dots.

eigenstate (2)1/2 is essentially spanned by $A\Sigma$. However at intermediate range 1.2–7.3 Å, (2)1/2 switches to $B\Pi$ which lies below $A\Sigma$. At $R =$ 8.1 Å it undergoes another avoided crossing and is finally adiabatically correlated with the lowest asymptote $2p_{1/2}$. Consistently, state (3)1/2 has a $B\Pi$ character at short distance, switches to $A\Sigma$ in the intermediate range and is adiabatically correlated with asymptote $2s_{1/2}$. Finally state (4)1/2 has essentially a $C\Sigma$ character for $R < 8.1$ Å, however as a consequence of the avoided crossing between the Σ state at 8.1 Å, it becomes adiabatically correlated with asymptote $2p_{3/2}$. Only state (1)3/2 remains identical to its parent state $B\Pi$ at all distances, except for an asymptotic shift. It should be noted that in a diabatic picture where the states may cross (but where the hamiltonian is no longer diagonal), three 1/2 states keeping the $A\Sigma$, $B\Pi$ and $C\Sigma$ character almost up to dissociation could be defined, correlated to $2p_{1/2}$, $2p_{3/2}$ and $2s_{1/2}$ respectively after multiple crossings.

The transition dipole moments (Fig. 6) between the spin-orbit states Ψ_m^{SO} can easily be determined from those computed between the quasi-diabatic CI wavefunctions,

$$\mathbf{D}_{mn}^{SO} = < \Psi_m^{SO} | \mathbf{D} | \Psi_n^{SO} > = \sum_{k\sigma, l\tau} c_{k\sigma}^m c_{l\tau}^n < \tilde{\Phi}_{k\sigma} | \mathbf{D} | \tilde{\Phi}_{l\tau} > \delta_{\sigma\tau}. \quad (4)$$

The dipole moments of transitions $X_{1/2} - (2)1/2$ and $X_{1/2} - (4)1/2$ show kinks at 8.1 Å, while that of the $X_{1/2} - (3)1/2$ transition changes sign. This feature results from the avoided or actual crossings between their three A, B, and C parents and the consecutive multiple crossings of the spin-orbit states at this distance. The transition moment $X_{1/2} - (1)3/2$ remains clearly equal to that of $X - B$. The dipole moments of transitions $X_{1/2} - (2)1/2$ and $X_{1/2} - (3)1/2$ furthermore show a sudden exchange at 1.2 Å due to the crossing of their parent states $A\Sigma$ and $B\Pi$, respectively, at that distance.

The electronic structure of HeH involving fine structure has also been investigated with pseudopotentials (Kielkopf 2021), in excellent agreement with our calculation in the region $R >$ 6 Å. Although we carried out an analysis of the effect of spin-orbit coupling on the H-He potential curves and transition moments, spin-orbit coupling is not taken into account in the collisional section below. The most important effect, namely the adiabatic correlation of the C state with the upper allowed 2p asymptote associated with a nonvanishing $X - C$ dipole moment, is maintained when spin-orbit coupling is accounted for: the $C_{1/2}$ state, spanned by the parent state $C\Sigma$ at short distance, correlates with the dipole-allowed atomic state $2p_{3/2}$, and the $X_{1/2} - (4)1/2$ transition dipole remains finite at large distance.

2.4. H-H potentials

In Allard et al. (1994) the theoretical potentials for the binary interaction of one hydrogen atom with another hydrogen atom were taken from the calculations of Sharp (1971) and Wolniewicz & Dressler (1988). The dependence of the probabilities of the allowed molecular transitions on internuclear separation contributing to the Lyman-α line were taken from Dressler & Wolniewicz (1985) for the singlet states and preliminary ab initio results for the transitions between the triplet states. The allowed transitions contributing to Lyman-α were summarized in Table 4 of Allard et al. (1994), but the labels of the a and h triplet states were interchanged. The symmetry and labeling of the H-H states are listed in Table 2. It might be wondered whether the inclusion of relativistic terms might seriously affect the long-distance behavior of the potentials and the transition dipole moments, as found in HHe. In Fig. 7 we show the long-range behavior of the theoretical quasi-full CI H-H potentials of Spielfiedel (priv. comm.) carried out in the Coulomb framework, and MRCI calculations (full CI) conducted on H-H with the same basis set as was used on hydrogen in HHe (see above) and the DKH correction. The splitting of the 2s and 2p levels also induces avoided crossings in H_2. While states $h^3\Sigma_g^+$ and $B'^1\Sigma_u^+$ join the asymptote around 15 Å states $a^3\Sigma_g^+$ and $B^1\Sigma_u^+$ remain significantly attractive up to very large separation because of the $1/R^3$ contribution. They exhibit avoided crossings (within each symmetry manifold) with the former states (diabatically correlated with atomic forbidden asymptotes). However, in H_2, these avoided crossings take place at very long distance, namely around $R = 45$ Å. At this interatomic separation, the electronic coupling vanishes and we can consider that in a collisional situation the system will follow a diabatic behavior, namely it will move along diabatic potentials that cross. In the present case with vanishing coupling, diabatic potentials can easily be defined by reassigning the adiabatic potential values before and after the (avoided) crossing.

Because only the difference potentials are meaningful for the treatment of collisional broadening, we can infer that scalar relativistic corrections are not needed and the potentials in the Coulomb description can be used simply as diabatic potentials. We therefore used the theoretical H-H potentials of Spielfiedel (priv. comm.) together with the electronic transition moments among singlets and triplets taken from Spielfiedel (2003) and Spielfiedel et al. (2004). As with H-He, spin-orbit coupling is not considered in the collisional section that follows.

3. Collisional profiles perturbed by neutral H and He atoms

Quasi-molecular lines in the red wing of Lyman-α, Lyman-β, and Lyman-γ arise from radiative collisions of excited atomic hydrogen with unexcited neutral hydrogen atoms or protons Allard & Kielkopf (1991); Allard et al. (1998b,a, 2000, 2004b,a, 2009). A general unified theory in which the electric dipole moment varies during a collision (Allard et al. 1999) is essential

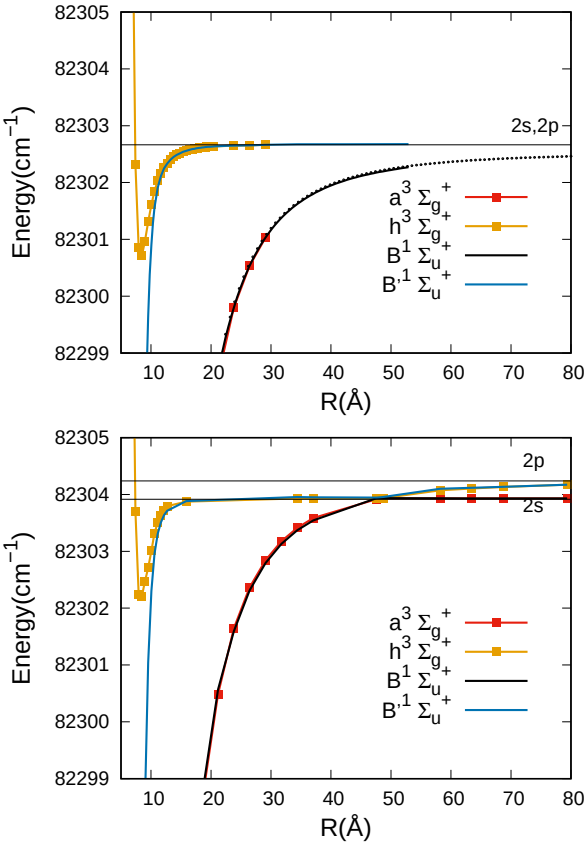

Fig. 7. Long-range zoom of the adiabatic potential energy curves of states $a^3\Sigma_g^+$, $h^3\Sigma_g^+$, $B^1\Sigma_u^+$, and $B'^1\Sigma_u^+$ of H+H($n=2$). *Top*: data of Spielfiedel et al. (priv. comm.) without scalar relativistic terms. *Bottom*: our CI results including the DKH correction. Zero energy corresponds to H(1s)+H(1s) at dissociation. The dotted line corresponds to the C_3/R^3 asymptotic extrapolation (hidden within the calculated curves lines in the bottom plot).

as the blue H-H quasi-molecular line satellite is due to an asymptotically forbidden transition $b\,^3\Sigma_u \rightarrow h\,^3\Sigma_g$.

3.1. Unified theory

Starting with the Anderson (1952) theory suitably generalized to include degeneracy, a unified theory of spectral line broadening (Allard et al. 1999) was developed to calculate neutral atom spectra, given the interaction and the radiative transition moments of relevant states of the radiating atom with other atoms in its environment. The unified profiles are the Fourier transforms (FT) of the autocorrelation functions as given by Eq. (121) of Allard et al. (1999), in which the contributions from the different components of a transition enter with their statistical weights. A pairwise additive assumption allows us to calculate $I(\Delta\omega)$, when N perturbers interact as the FT of the Nth power of the autocorrelation function $\phi(s)$ of a unique atom-perturber pair. For a perturber density n_p, we obtain

$$\Phi(s) = e^{-n_p g(s)}, \tag{5}$$

where the decay of the autocorrelation function with time leads to atomic line broadening.

For a transition $\alpha = (i, f)$ from an initial state i to a final state f, we have

$$g_\alpha(s) = \frac{1}{\sum_{e,e'}{}^{(\alpha)} |d_{ee'}|^2} \sum_{e,e'}^{(\alpha)} \int_0^{+\infty} 2\pi\rho d\rho \int_{-\infty}^{+\infty} \mathrm{d}x\, \tilde{d}_{ee'}[R(0)] \left[e^{\frac{i}{\hbar}\int_0^s \mathrm{d}t\, V_{e'e}[R(t)]}\, \tilde{d}^*_{ee'}[R(s)] - \tilde{d}_{ee'}[R(0)] \right]. \tag{6}$$

In Eq. (6) the symbols e and e' label the energy surfaces on which the interacting atoms approach the initial and final atomic states of the transition. The sum $\sum_{e,e'}^{(\alpha)}$ is over all pairs (e, e') such that $\omega_{e',e}(R) \rightarrow \omega_\alpha$ as $R \rightarrow \infty$. In the equations that follow, we review the meaning of these terms in Eq. (6). In our context, the perturbation of the frequency of the atomic transition during the collision results in a phase shift, $\eta(s)$, which is calculated along a classical path $R(t)$ that is assumed to be rectilinear. At time t from the point of closest approach, the atoms are separated by

$$R(t) = \left[\rho^2 + (x + \bar{v}t)^2\right]^{1/2}, \tag{7}$$

where ρ is the impact parameter of the perturber trajectory, $\bar{v}$ is the relative velocity, and x the position of the perturber along its trajectory at time $t = 0$. We have for the phase term in Eq. (6)

$$\eta(s) = \frac{i}{\hbar} \int_0^s \mathrm{d}t\, V_{e'e}[R(t)], \tag{8}$$

where $\Delta V(R)$, the difference potential, is given by

$$\Delta V(R) \equiv V_{e'e}[R(t)] = V_{e'}[R(t)] - V_e[R(t)], \tag{9}$$

and represents the difference between the energies of the quasi-molecular transition. The potential energy for a state e is

$$V_e[R(t)] = E_e[R(t)] - E_e^\infty. \tag{10}$$

3.2. Satellite bands due to H-H and H-He

Within the assumption of additive superposition of interactions, we can write the total profile as the convolution of the individual profiles corresponding to perturbations by H and He,

$$I_{\mathrm{tot}}(\Delta\omega) = I_{\mathrm{H-H}}(\Delta\omega) * I_{\mathrm{H-He}}(\Delta\omega). \tag{11}$$

The unified theory (Allard & Kielkopf 1982) predicts that line satellites are centered periodically at frequencies corresponding to integer multiples of the extrema of $\Delta V(R)$ (Eq. (9)). However, their appearance depends on the value of the electronic dipole moments in the region of the maximum of $\Delta V(R)$ (Allard et al. 1998a).

The prediction of the shape of the blue wing required us to study the potential energies of the two triplet transitions $b\,^3\Sigma_u^+ \rightarrow h\,^3\Sigma_g^+$ and $b\,^3\Sigma_u^+ \rightarrow i\,^3\Pi_g$ that contribute to the blue wing of the Lyman-α line (Fig. 8). For comparison we overplot the potential energies of the $X\,\Sigma$ and $C\,\Sigma$ states of the H-He system. The prediction of a line satellite in the blue wing of the H-H and H-He line profiles is related to the potential maximum at short distance $R = 2$–3 Å of the C, h, and i states. This leads to a maximum of the potential energy difference $\Delta V(R)$ for these transitions shown in Fig. 9. The electronic states h and b of the isolated radiator are not connected by the dipole moment operator: $d_{hb}(R \rightarrow \infty) = 0$. As reported in Spielfiedel et al. (2004),

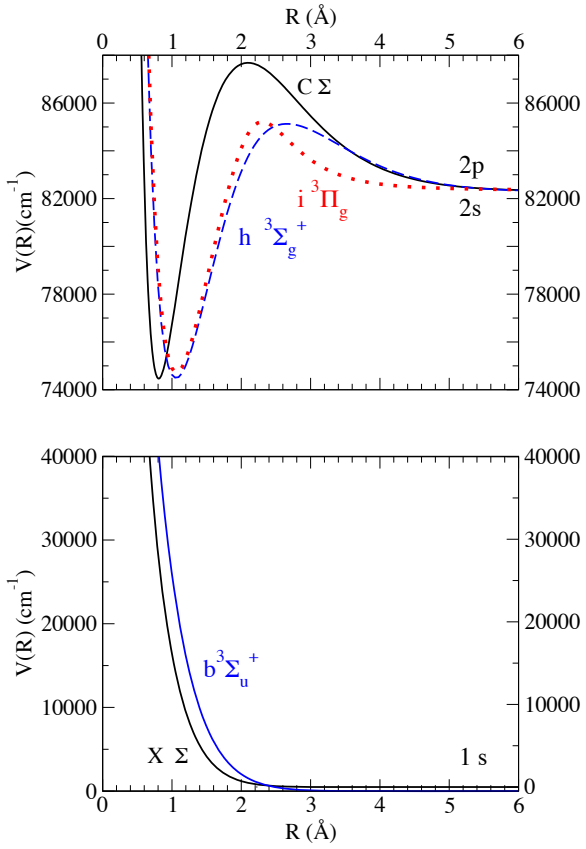

Fig. 8. *Top*: short-range part of the repulsive potential curve $C\Sigma$ (black line) of the H-He molecule compared to the $h\ ^3\Sigma_g^+$ (dashed blue line) and $i\ ^3\Pi_g$ (dashed red line) states of the H_2 molecule. *Bottom*: X (black line) and $b\ ^3\Sigma_u^+$ (blue line).

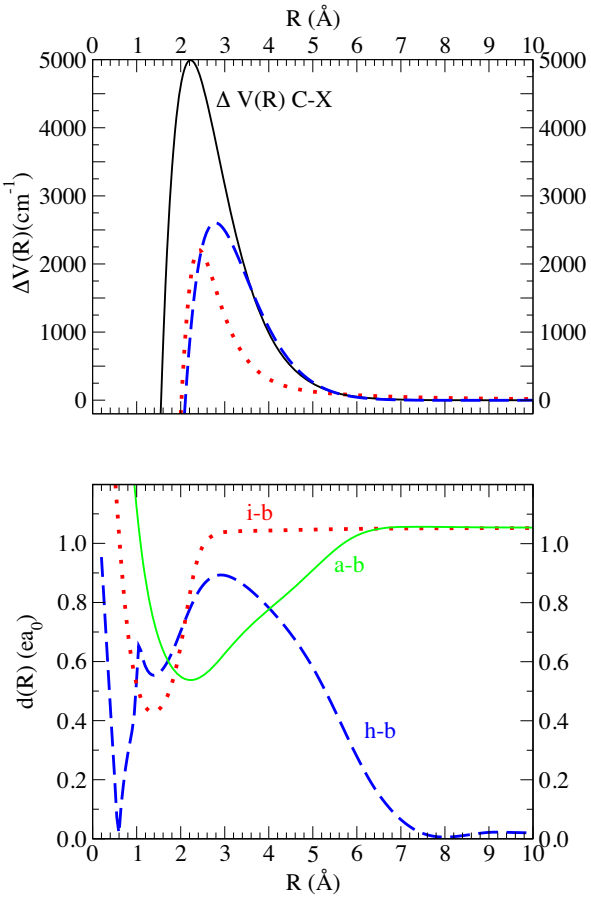

Fig. 9. *Top*: difference potential for the triplet transitions $h - b$ (dashed blue line), $i - b$ (dotted red line) of H-H compared to the $X - C$ transition of H-He. *Bottom*: electric dipole transition moments between the triplet states of H-H. The $h - b$ transition is forbidden asymptotically as it is a transition between the 2s and 1s states of the free hydrogen atom at large R.

the 2, 3 $^3\Sigma_g$ states (labeled h, a) undergo an avoided crossing at equilibrium distance and thus exchange their character. The radiative dipole moment varies dramatically with R (bottom of Fig. 9). Allowed radiative transitions cannot occur between these two states, but $d_{hb}(R)$ differs from zero when a perturber passes close to the radiator. Our theoretical approach allows us to take this asymptotically forbidden transition $b^3\Sigma_u^+ \rightarrow h^3\Sigma_g^+$ of quasi-molecular hydrogen that dissociates into (1s, 2s) atoms into account. An other important factor is the variation of the dipole moment during the collision once modulated by the Boltzmann factor $e^{-\beta V_e(r)}$ (Eq. (117) of Allard et al. 1999),

$$D(R) = \tilde{d}_{if}[R(t)] = d_{if}[R(t)]e^{-\frac{V_e[R(t)]}{2kT}} \quad . \tag{12}$$

The Boltzmann factor $e^{-\frac{V_e(R)}{2kT}}$ in Eq. (12) appears because the perturbing atoms are in thermal equilibrium with the radiating atom, which affects the probability of finding them initially at a given R. In this case, where we consider absorption profiles due to triplet transitions, V_e is the $b\ ^3\Sigma_u^+$ ground-state potential. In Fig. 10 we show $D(R)$ together with the corresponding $\Delta V(R)$ for the h-b transition. The dipole moment $D(R)$ and the energy difference determining the transition wavelength $\Delta V(R)$ are maximum at $R_{\rm ext}$= 2.8 Å. In this instance, a radiative transition is induced by collisions. Figure 10 shows that $D(R)$ is not dependent on temperature throughout the region where the collision-induced satellite is formed, and therefore the blue wing of Lyman-α will not change with increasing temperature in the range of temperatures 10 000–15 000 K.

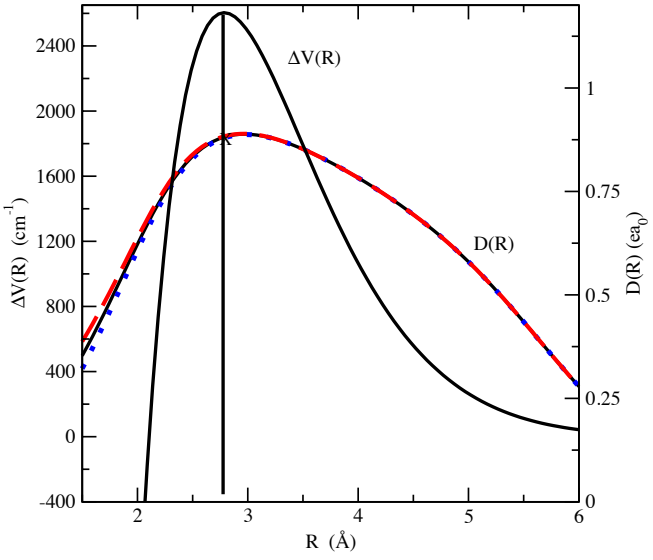

Fig. 10. Variation with temperature in the modulated dipole and the difference potential of the triplet state h-b of the H-H molecule. T = 15 000 K (dashed red line), T = 12 000 K (black line), and T = 10 000 K (dotted blue line).

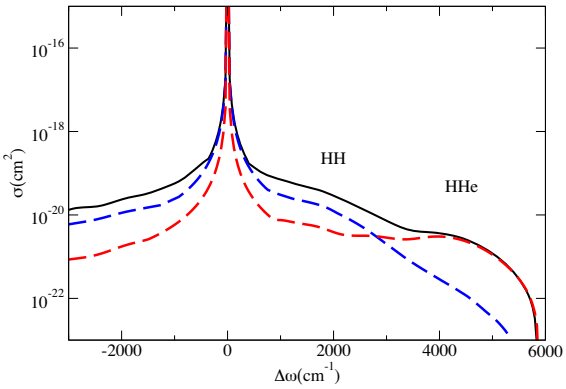

Fig. 11. Blue wings of Lyman-α due to H-H collisions (blue curve), H-He collisions (dashed red curve), and simultaneous collisions by H and He (black curve). The H and He densities are 10^{18} cm^{-3}, and the temperature is 12 000 K.

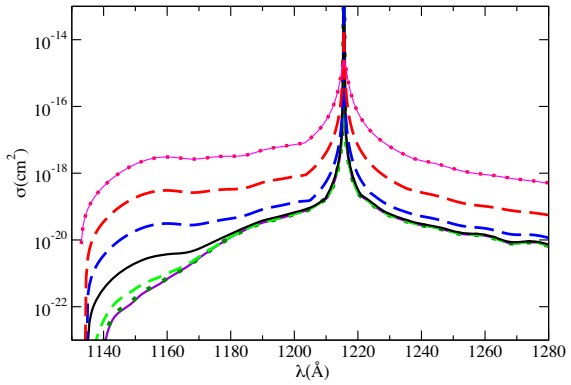

Fig. 12. Blue wing of Lyman-α simultaneously perturbed by He and H atoms for a different ratio of helium and hydrogen densities. From top to bottom, n_{He}/n_H is 10^3, 10^2, 10, 1, 0.1, and 10^{-2}. The Lyman-α profiles resulting from perturbation by either H-He or H-H collisions separately are overplotted (dotted lines) for ratios of 10^3 and 10^{-2}, respectively. The temperature is 12 000 K.

An examination of Fig. 9 leads us to expect a farther blue satellite for H-He that arises from the extremum of 5000 cm^{-1} when the two atoms are separated by about 2 Å compared to 2100–2500 cm^{-1} for $i-b$ and $h-b$. Figure 11 shows the distinct wide satellite at about 4200 cm^{-1} owing to the X-C transition, whereas the $b\,^3\Sigma_u^+ \rightarrow h\,^3\Sigma_g^+$ transition yields a blue shoulder centered approximately at 1900 cm^{-1} in the blue wing of Lyman-α of H-H. Although $\Delta V(R)$ for the allowed transition $b\,^3\Sigma_u \rightarrow i\,^3\Sigma_u$ has a maximum (ΔV= 2100 cm^{-1}), it simply contributes to the blue asymmetry as it is blended in the near wing.

The wavelength of the theoretical collision-induced satellite is largely dependent on the accuracy of the difference potential of the two contributing states to the transition, while the strength of the absorption as a function of wavelength is dependent on the radiative dipole moment shown in Fig. 10 and on the accuracy of the spectral line shape theory. This line satellite has been observed experimentally in the spectrum of a laser-produced plasma source, see Fig. 2 of Kielkopf & Allard (1995) and Fig. 7 of Kielkopf & Allard (1998).

3.3. Collisional profiles simultaneaously perturbed by He and H atoms

The spectra of helium-dominated white dwarf stars with hydrogen in their atmosphere present a distinctive broad feature centered around 1160 Å in the blue wing of the Lyman-α line (see Fig. 1 in Allard et al. 2020). Figure 11 shows that this line satellite is quite close to the one due to H-H collisions centered at 1190 Å. We caused the ratio n_{He}/n_H of their densities to vary. Line profiles that are simultaneously perturbed by H and He are computed for a ratio varying from 10^{-2} to 10^3, and the H density n_H remains equal to 10^{18}cm^{-3}. When the ratio is 10^3, the H-He line profile is identical to a pure helium profile, whereas for 10^{-2}, the H-He line satellite at 1160 Å is not seen. This is illustrated in Fig. 12. The blue wings of Lyman-α perturbed by He or H atoms are compared in Fig. 13. The line profile calculations were made at a temperature of 12 000 K for a perturber density of 10^{18} cm^{-3} of He or neutral H. An additional feature is shown in the blue wing of H-H Lyman-α at 1150 Å. This feature is a line satellite of Lyman-β quite far from the unperturbed Lyman-β line center; it is even closer to the Lyman-α line. Figure 13 shows that it is therefore necessary to take the total contribution of the Lyman-α and Lyman-β wings of neutral H throughout this region into account.

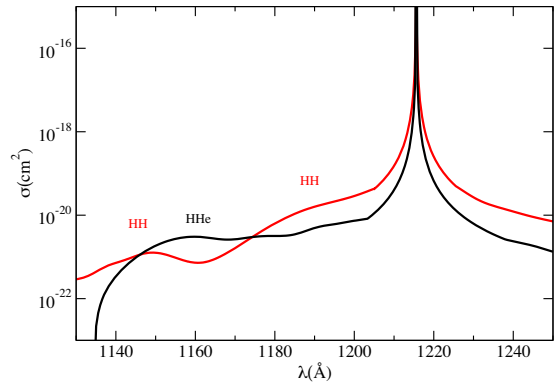

Fig. 13. Comparison of the blue wings of Lyman-α perturbed by H-He collisions (black curve) with the blue wing in the Lyman-α range (red curve) due to H-H collisions. The contribution of the red wing of Lyman-β leads to a large feature at 1150 Å. The H and He densities are 10^{18} cm^{-3}, and the temperature is 12 000 K.

3.4. Observation of the 1150 Å satellite

This absorption feature due to the $B''\bar{B}\,^1\Sigma_u^+$ - $X\,^1\Sigma_g^+$ transition was predicted by Allard et al. (2000). The ab initio calculations of Spielfiedel (2003) have shown that for the isolated radiating atom ($R \rightarrow \infty$), this transition is not asymptotically forbidden, as was explicitly stated in Allard et al. (2000).

We reported a theoretical study of the variation of the Lyman-β profile with the relative density of ionized and neutral atoms and demonstrated that a ratio of 5 of the neutral and proton density is enough to make this line satellite appear in the far wing (Fig. 5 of Allard et al. 2000). The line satellite appearance is then very sensitive to the degree of ionization and may be used as a temperature diagnostic. In Allard et al. (2004a) we reported its first detection in far-UV (FUV) observations of the pulsating DA white dwarf G226−29 obtained with the Far Ultraviolet Spectroscopic Explorer (FUSE). This broad feature was also detected in the laboratory by Kielkopf et al. (2004) and observed in another variable DA star, G185-32, by Dupuis et al. (2006).

In Allard et al. (2004c) we discussed in detail how important it is to take the Boltzmann factor in absorption into account in Eq. (12), especially in stellar atmospheres for temperatures lower than 15 000 K. We considered local thermal equilibrium model

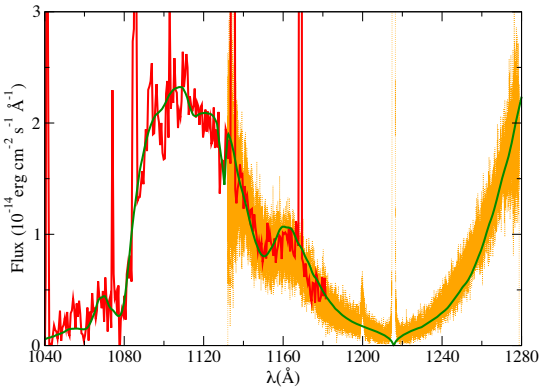

Fig. 14. Comparison of the synthetic spectrum obtained with $T_{\rm eff}$ = 12 040 K and $\log g$ = 7.93 (green line) in the Lyman-β range with a FUSE spectrum of G226-29 (red line; extracted from Fig. 5 of Allard et al. 2004c). We overplot the COS observation of G226-29 (Gaensicke 2016; orange line).

atmospheres with a pure hydrogen composition that explicitly include the Lyman-α and Lyman-β quasi-molecular opacities. For the case of G226-29 shown in Fig. 14, we used a very high signal-to-noise ratio (S/N) spectrum obtained using time-resolved HST spectra presented by Kepler et al. (2000). This comparison allowed us to make a temperature and gravity determination that is compatible with a fit to the FUSE observation of this object. Figure 4 of Allard et al. (2004a) showed our fit to the HST spectrum using our adopted values for $T_{\rm eff}$ = 12 040 K and $\log g$ = 7.93. We extracted data from Fig. 5 of Allard et al. (2004c), where synthetic spectra in the Lyman-β range are compared with a FUSE spectrum of G226-29, to show in Fig. 14 the synthetic spectrum obtained for T = 12 040 K and $\log g$ = 7.93. G226-29 was more recently observed with HST COS under program 14 076, and we overplot the spectrum of the G130M$_2$ grating that covers 1130–1270 Å. The HST COS observation is noisy but consistent with the one obtained by FUSE and fills the gap above 1180 Å where the shoulder in the blue wing of Lyman-α appears. This part of the spectrum 1180–1200 Å could not be obtained with FUSE or HST. However, we should point out that we need to divide the COS flux by a factor of ∼1.3 to bring it to the FUSE spectrum, we had a similar problem in Allard et al. (2004a) to fit the FUSE and IUE flux. We considered that this difference by a factor of ∼1.3 in the flux calibration of observations performed with two different instruments of a faint target was acceptable, but obtaining the same factor with COS would mean that the error is likely due to FUSE.

4. Conclusions

The effect of collision broadening by atomic H and He on spectral lines is central for understanding the opacity of stellar atmospheres. A correct determination of the Lyman-α line requires the determination of the ground and first excited potential energy curves and the electric transition dipole moments with high accuracy. We showed for H-He how important it is to account for relativistic effects to characterize the long-distance behavior of the potentials in detail and the avoided crossing situations. These effects, although tiny, become crucial in determining the character and the adiabatic correlation of the states, and in particular, the behavior of the associated dipole transition moments from the ground state, because of the specific degeneracy of hydrogen-excited states in the Coulomb model. This problem does not seem so stringent for H+H (n = 2) collisions. Due to the $1/R^3$ asymptotic behavior of the states that also undergo avoided crossings, but at very large separation, in this case, the behavior of the system is expected to be fully diabatic, except perhaps in ultra-cold and ultra-slow systems.

Our study was conducted assuming classical motion for the nuclei, as well as an adiabatic picture for the electronic states during the collisional process. The so-called diagonal adiabatic corrections (Kolos & Wolniewicz 1968; Pachucki & Komasa 2014; Komasa et al. 1999; Gherib et al. 2016), which mostly contribute at short distance, might also be added for an improved accuracy. Moreover, it should be mentioned that in the regions in which the potential curves of different states are very close, such as at large separation especially in the H-He case or in short-range avoided crossing regions such as in H-H, the Born-Oppenheimer approximation defining the adiabatic states is likely to break down, and it might be necessary to take off-diagonal nonadiabatic couplings and collisional branchings between the adiabatic states into account. Lique et al. (2004) took the rotational coupling between states $B^1\Sigma_u^+$ and $C^1\Pi_u$ in H-H collisions into account and concluded that the nonadiabatic effects with respect to the adiabatic treatment were very weak in this case. The effect of nonadiabatic couplings remains an open question in the triplet case, which presents avoided crossings at short distance.

The HST observations have motivated this theoretical work, in which we used accurate molecular data for both the HH (Spielfiedel 2003; Spielfiedel et al. 2004) and HHe (this work) and extended that of Allard et al. (2020). This allowed a thorough study of the atomic underlying atomic physics and accurate line profile calculations of Lyman lines perturbed by collisions with H and He atoms given here. Furthermore, it is also very gratifying to observe features that have been predicted theoretically. This was the case of the 1150 Å broad feature in the Lyman-β wing of the FUSE spectrum of the DA white dwarf G226-29 and now this one at 1160 Å in the blue wing of COS spectra of DBA white dwarfs. The COS observation of G226-29 was also an opportunity to reconsider the blue wing of Lyman-α. Finally, our study is a first step toward obtaining the accurate data for both Lyman-α and for Balmer-α that are essential for determining the hydrogen abundance correctly.

References

Allard, N. F., & Christova, M. 2009, New Astron. Rev., 53, 252
Allard, N. F., & Kielkopf, J. F. 1982, Rev. Mod. Phys., 54, 1103
Allard, N. F., & Kielkopf, J. F. 1991, A&A, 242, 133
Allard, N. F., & Kielkopf, J. F. 2009, A&A, 493, 1155
Allard, N. F., Koester, D., Feautrier, N., & Spielfiedel, A. 1994, A&AS, 108, 417
Allard, N. F., Drira, I., Gerbaldi, M., Kielkopf, J. F., & Spielfiedel, A. 1998a, A&A, 335, 1124
Allard, N. F., Kielkopf, J. F., & Feautrier, N. 1998b, A&A, 330, 782
Allard, N. F., Royer, A., Kielkopf, J. F., & Feautrier, N. 1999, Phys. Rev. A, 60, 1021
Allard, N. F., Kielkopf, J., Drira, I., & Schmelcher., P. 2000, Eur. Phys. J. D, 12, 263
Allard, N. F., Hébrard, G., Dupuis, J., et al. 2004a, ApJ, 601, L183
Allard, N. F., Kielkopf, J. F., Hébrard, G., & Peek, J. 2004b, Eur. Phys. J. D, 29, 7
Allard, N. F., Kielkopf, J. F., & Loeillet, B. 2004c, A&A, 424, 347
Allard, N. F., Noselidze, I., & Kruk, J. W. 2009, A&A, 506, 993
Allard, N. F., Kielkopf, J. F., Xu, S., et al. 2020, MNRAS, 494, 868
Anderson, P. W. 1952, Phys. Rev., 86, 809
Belyaev, A. K. 2015, Phys. Rev. A, 91, 062709
Bergeron, P., Wesemael, F., Lamontagne, R., et al. 1995, ApJ, 449, 258
Cohen, J. S., & Schneider, B. 1974, J. Chem. Phys., 61, 3230

Dressler, K., & Wolniewicz, L. 1985, J. Chem. Phys., 82, 4720
Dupuis, J., Allard, N. F., Hébrard, G., et al. 2006, ASP Conf. Ser., 348, 200
Gaensicke, B. 2016, Data from HST proposal 14076 – White Dwarf Stars, MAST archive
Gherib, R., Ye, L., Ryabinkin, I. G., & Izmaylov, A. F. 2016, J. Chem. Phys., 144, 154103
Kepler, S. O., Robinson, E. L., Koester, D., et al. 2000, ApJ, 539, 379
Ketterle, W., Figger, H., & Walther, H. 1985, Phys. Rev. Lett., 55, 2941
Ketterle, W., Dodhy, A., & Walther, H. 1988, J. Chem. Phys., 89, 3442
Kielkopf, J. 2021, Valence electron-noble gas atom pseudopotentials for atomic line shape calculations, https://github.com/sharedskies/pseudopotential, [Online; accessed 2021-04-06]
Kielkopf, J. F., & Allard, N. F. 1995, ApJ, 450, L75
Kielkopf, J. F., & Allard, N. F. 1998, Phys. Rev. A, 58, 4416
Kielkopf, J. F., Allard, N. F., & Huber, J. 2004, ApJ, 611, L129
Knowles, P., & Werner, H.-J. 1992, Theor. Chim. Acta, 84, 95
Koester, D., Allard, N. F., & Vauclair, G. 1994, A&A, 291, L9
Kolos, W., & Wolniewicz, L. 1968, J. Chem. Phys., 49, 404
Komasa, J., Cencek, W., & Rychlewski, J. 1999, Chem. Phys. Lett., 304, 293
Kramida, A.-E. 2010, At. Data Nucl. Data Tables, 96, 586
Kramida, A., Yu. Ralchenko, Reader, J., & NIST ASD Team. 2020, NIST Atomic Spectra Database (ver. 5.8), [Online]. Available: https://physics.nist.gov/asd [2021, January 26]. National Institute of Standards and Technology, Gaithersburg, MD.
Lique, F., Tchang-Brillet, W.-Ü. L., Spielfiedel, A., & Feautrier, N. 2004, J. Phys. B At. Mol. Phys., 37, 3021
Lo, J. M. H., Klobukowski, M., Bielińska-Waz, D., Schreiner, E. W. S., & n, G. H. F. D. 2006, J. Phys. B At., Mol. Opt. Phys., 39, 2385
Nakajima, T., & Hirao, K. 2011, Chem. Rev., 112, 385
Pachucki, K., & Komasa, J. 2014, J. Chem. Phys., 141, 224103
Reiher, M. 2006, Theor. Chem. Acc., 116, 241
Sarpal, B. K., Branchett, S. E., Tennyson, J., & Morgan, L. A. 1991, J. Phys. B At., Mol. Opt. Phys., 24, 3685
Sharp, T. E. 1971, At. Data, 2, 119
Spielfiedel, A. 2003, J. Mol. Spectr., 217, 162
Spielfiedel, A., Palmieri, P., & Mitrushenkov, A. 2004, Mol. Phys., 102, 2249
Theodorakopoulos, G., Farantos, S. C., Buenker, R. J., & Peyerimhoff, S. D. 1984, J. Phys. B At. Mol. Phys., 17, 1453
Theodorakopoulos, G., Petsalakis, I. D., Nicolaides, C. A., & Buenker, R. J. 1987, J. Phys. B, 20, 2339
Werner, H.-J., Knowles, P. J., Knizia, G., et al. 2015, MOLPRO, version 2015.1, a package of ab initio programs
Wolniewicz, L., & Dressler, K. 1988, J. Chem. Phys., 88, 3861
Xu, S., Zuckerman, B., Dufour, P., et al. 2017, ApJ, 836, L7

Appendix A: Additional tables

Table A.1. Exponents of Gaussian-type functions on hydrogen added to the aug-cc-pV6Z basis set.

s	0.03,0.008,0.006902040, 0.0035, 0.00175,0.0008
p	0.12,0.030, 0.015, 0.007,0.0035,0.00175,0.0008
d	0.055406537, 0.024364162, 0.010713761,0.005,0.0025,0.0012
f	0.106396067, 0.046204584, 0.020065249,0.008,0.006,0.0035,0.0015
g	0.168703345, 0.069928301, 0.028985598
h	0.175320015, 0.045069073, 0.011585793

Notes. The three first exponents of d, f, g, and h functions are taken from Allard et al. (2020).

Table A.2. Spectroscopic constants of the molecular states dissociating into H(2s,2p)+He($1s^2$).

State	ref.	R_e(Å)	ω_e(cm^{-1})	D_e(cm^{-1}/eV)
$A\Sigma$	(a)	0.74022	3730.3	20 658 (2.561)
	(b)	0.74074	3697.2	(2.563
	(c)	0.7472	3726	(2.54)
	(d)	0.7430	3512	
	(e)	0.7573	3662	
	(f)	0.7567	3701	
	(g)	0.74 086	3718	
$B\Pi$	(a)	0.76813	3339.9	17 868.4 (2.218)
	(b)	0.76863	3313.4	(2.218)
	(c)	0.7738	3372	(2.20)
	(d)	0.7711	3158	
	(e)	0.7741	3302	(2.20)
$C\Sigma$	(a)	0.80927	2916.5	13 665.5 (1.694)
	(b)	0.80953	2906.3	(1.638)
	(c)	0.8133	2957	(1.61)
	(d)	0.8073	2788	
	(e)	0.81641	2872	(1.65)
	(f)	0.8308	2896	
	(g)	0.8109	2902	

Notes. D_e values in parentheses are in eV. The dissocation energy of state $C\Sigma$ is taken below the barrier top lying 5386 cm^{-1} above the dissociation limit H(2s,2p)+He. (a) this work, (b) theory, Allard et al. (2020), (c) theory, Lo et al. (2006), (d) theory, Sarpal et al. (1991), (e) theory, Theodorakopoulos et al. (1987), (f) experimental spectroscopy, Ketterle et al. (1985), and (g) experimental spectroscopy, Ketterle et al. (1988).